

1 **Long term variations of actual evapotranspiration over the Tibetan**  
2 **Plateau**

3 Cunbo Han<sup>1,2,3</sup>, Yaoming Ma<sup>1,4,5,6</sup>, Binbin Wang<sup>1,2</sup>, Lei Zhong<sup>7</sup>, Weiqiang  
4 Ma<sup>1,2,4</sup>, Xuelong Chen<sup>1,2,4</sup>, Zhongbo Su<sup>8</sup>

5 1. Key Laboratory of Tibetan Environment Changes and Land Surface  
6 Processes, Institute of Tibetan Plateau Research, Chinese Academy of  
7 Sciences, Beijing, China

8 2. Land-Air Interaction and Climate Effect Group, State Key Laboratory of  
9 Tibetan Plateau Earth System Science, Institute of Tibetan Plateau  
10 Research, Chinese Academy of Sciences, Beijing, China

11 3. Institute for Meteorology and Climate Research, Karlsruhe Institute of  
12 Technology, Karlsruhe, Germany

13 4. CAS Center for Excellence in Tibetan Plateau Earth Sciences, Chinese  
14 Academy of Sciences, Beijing, China

15 5. University of Chinese Academy of Sciences, Beijing, China

16 6. Lanzhou University, Lanzhou, China

17 7. Laboratory for Atmospheric Observation and Climate Environment  
18 Research, School of Earth and Space Sciences, University of Science  
19 and Technology of China, Hefei, China

20 8. Faculty of Geo-Information Science and Earth Observation, University of  
21 Twente, Enschede, The Netherlands

22

23 **Correspondence to:**

24 Prof. Dr. Yaoming Ma

25 Institute of Tibetan Plateau Research, Chinese Academy of Sciences

26 16-3 Lincui Road, Chaoyang District, Beijing, 100101, China

27 Tel: +86 010 84097079

28 Email: [ymma@itpcas.ac.cn](mailto:ymma@itpcas.ac.cn)

29 **Abstract**

30 Terrestrial actual evapotranspiration ( $ET_a$ ) is a key parameter controlling land-  
31 atmosphere interaction processes and the water cycle. However, spatial  
32 distribution and temporal changes of  $ET_a$  over the Tibetan Plateau (TP)  
33 remain very uncertain. Here we estimate the multiyear (2001-2018) monthly  
34  $ET_a$  and its spatial distribution on the TP by a combination of meteorological  
35 data and satellite products. Validation against data from six eddy-covariance  
36 monitoring sites yielded root-mean-square errors ranging from 9.3 to 14.5 mm  
37  $mo^{-1}$ , and correlation coefficients exceeding 0.9. The domain mean of annual  
38  $ET_a$  on the TP decreased slightly ( $-1.45 \text{ mm yr}^{-1}$ ,  $p < 0.05$ ) from 2001 to 2018.  
39 The annual  $ET_a$  increased significantly at a rate of  $2.62 \text{ mm yr}^{-1}$  ( $p < 0.05$ ) in  
40 the eastern sector of the TP ( $lon > 90^\circ \text{ E}$ ), but decreased significantly at a rate  
41 of  $-5.52 \text{ mm yr}^{-1}$  ( $p < 0.05$ ) in the western sector of the TP ( $lon < 90^\circ \text{ E}$ ). In  
42 addition, the decreases in annual  $ET_a$  were pronounced in spring and summer  
43 seasons, while almost no trends were detected in the autumn and winter  
44 seasons. The mean annual  $ET_a$  during 2001-2018 and over the whole TP was  
45  $496 \pm 23 \text{ mm}$ . Thus, the total evapotranspiration from the terrestrial surface of  
46 the TP was  $1238.3 \pm 57.6 \text{ km}^3 \text{ yr}^{-1}$ . The estimated  $ET_a$  product presented in  
47 this study is useful for an improved understanding of changes in energy and  
48 water cycle on the TP. The dataset is freely available at the Science Data  
49 Bank (<http://www.dx.doi.org/10.11922/sciencedb.t00000.00010>, (Han et al.,  
50 [2020](#))) and at the National Tibetan Plateau Data Center  
51 (<https://data.tpdc.ac.cn/en/data/5a0d2e28-ebc6-4ea4-8ce4-a7f2897c8ee6/>).

52

53 **Key words:** Actual evapotranspiration; SEBS; Tibetan Plateau; Trend.

54

55

56 **Key points:**

- 57       • The SEBS-estimated monthly  $ET_a$  during 2001-2018 has been  
58       validated against 6 flux towers on the TP.
- 59       • Annual  $ET_a$  over the entire TP and in the western TP decrease  
60       significantly, while it increases in the eastern TP.
- 61       • Decrease of annual  $ET_a$  is pronounced in spring and summer, while  
62       almost no trends are detected in autumn and winter.

63

64

## 65 1 Introduction

66 As the birthplace of Asia's major rivers, the Tibetan Plateau (TP), famous as  
67 the "Water Tower of Asia", is essential to the Asian energy and water cycles  
68 ([Immerzeel et al., 2010](#); [Yao et al., 2012](#)). Along with increasing air  
69 temperature, evidence from the changes of precipitation, runoff, and soil  
70 moisture indicates that the hydrological cycle of the TP has been intensified  
71 during the past century ([Yang et al., 2014](#)). Consuming around two-thirds of  
72 global terrestrial precipitation, evapotranspiration (*ET*) is a crucial component  
73 that affects the exchange of water and energy between the land surface and  
74 the atmosphere ([Oki and Kanae, 2006](#); [Fisher et al., 2017](#)). *ET* is also a key  
75 factor modulating regional and global weather and climate. As one essential  
76 connecting component between the energy budget and the water cycle in the  
77 terrestrial ecosystems ([Xu and Singh, 2005](#)), *ET* and its variations have been  
78 drawing more attention worldwide ([Xu and Singh, 2005](#); [Li et al., 2014](#); [Zhang](#)  
79 [et al., 2018b](#); [Yao et al., 2019](#); [Wang et al., 2020b](#)). Total evaporation from  
80 large lakes of the TP has been quantitatively estimated recently ([Wang et al.,](#)  
81 [2020a](#)), however, the terrestrial *ET* on the TP and its spatial and temporal  
82 changes remain very uncertain.

83

84 Many studies have tried to evaluate *ET*'s temporal and spatial variability  
85 across the TP using various methods. The pan evaporation ( $E_{\text{pan}}$ ), that  
86 represents the amount of water evaporated from an open circular pan, is the  
87 most popular observational data source of *ET*. Long time series of  $E_{\text{pan}}$  are  
88 often available with good comparability among various regional  
89 measurements. Thus, it has been widely used in various disciplines, e.g.,  
90 meteorology, hydrology, and ecology. Several studies have revealed the trend  
91 of  $E_{\text{pan}}$  on the TP ([Zhang et al., 2007](#); [Liu et al., 2011](#); [Shi et al., 2017](#); [Zhang](#)  
92 [et al., 2018a](#); [Yao et al., 2019](#)). Although  $E_{\text{pan}}$  and potential *ET* suggest the

93 long-term variability of  $ET$  according to the complementary relationship (CR)  
94 between  $E_{pan}$  and actual  $ET$  ( $ET_a$ ) ([Zhang et al., 2007](#)), these measures  
95 cannot precisely depict the spatial pattern of trends in  $ET_a$ . Recently, several  
96 studies applied revised models, which are based on the CR of  $ET$ , to estimate  
97  $ET_a$  on the TP ([Zhang et al., 2018b](#); [Ma et al., 2019](#); [Wang et al., 2020b](#)).  
98 Employing only routine meteorological observations without requiring any  
99 vegetation and soil information is the most significant advantage of CR  
100 models ([Szilagyi et al., 2017](#)). However, numerous assumptions and  
101 requirements of validations of key parameters limit the application and  
102 performance of CR models over different climate conditions. The application  
103 of eddy-covariance (EC) technologies in the past decade has dramatically  
104 advanced our understanding of the terrestrial energy balance and  $ET_a$  over  
105 various ecosystems across the TP. However, the fetch of the EC observation  
106 is on the order of hundreds of meters, thus impeding the ability to capture the  
107 plateau-scale variations of  $ET_a$ . Therefore, finding an effective way to advance  
108 the estimation of  $ET_a$  on the TP is of great importance.

109

110 Satellite remote sensing (RS) provides temporally frequent and spatially  
111 contiguous measurements of land surface characteristics that affect  $ET$ , for  
112 example, land surface temperature, albedo, vegetation index. Satellite RS  
113 also offers the opportunity to retrieve  $ET$  over a heterogeneous surface  
114 ([Zhang et al., 2010](#)). Multiple RS-based algorithms have been proposed.  
115 Among these algorithms, the surface energy balance system (SEBS)  
116 proposed by [Su \(2002\)](#) has been widely applied to retrieve land surface  
117 turbulent fluxes on the TP ([Chen et al., 2013b](#); [Ma et al., 2014](#); [Han et al.,](#)  
118 [2016](#); [Han et al., 2017](#); [Zou et al., 2018](#); [Zhong et al., 2019](#)). [Chen et al.](#)  
119 [\(2013b\)](#) improved the roughness length parameterization scheme for heat  
120 transfer in SEBS to expand its modeling applicability over bare ground, sparse

121 canopy, dense canopy, and snow surfaces in the TP. An algorithm for effective  
122 aerodynamic roughness length had been introduced into the SEBS model to  
123 parameterize subgrid-scale topographical form drag ([Han et al., 2015](#); [Han et](#)  
124 [al., 2017](#)). This scheme improved the skill of the SEBS model in estimating  
125 the surface energy budget over mountainous regions of the TP. A recent  
126 advance by [Chen et al. \(2019\)](#) optimized five critical parameters in SEBS  
127 using observations collected from 27 sites globally, including 6 sites on the TP,  
128 and suggested that the overestimation of the global  $ET$  was substantially  
129 improved with the use of optimal parameters.

130

131 While the spatial and temporal pattern of the  $ET_a$  in the TP had been  
132 investigated in many studies ([Zhang et al., 2007](#); [Zhang et al., 2018b](#); [Wang](#)  
133 [et al., 2020b](#)), considerable inconsistencies for both trends and magnitudes of  
134  $ET_a$  exist due to uncertainties in forcing and parameters used by various  
135 models. Thus, in this study, with full consideration of the recent developments  
136 in the SEBS model over the TP, we aim to (1) develop an 18-year (2001-2018)  
137  $ET_a$  product of the TP, along with independent validations against EC  
138 observations; (2) quantify the spatiotemporal variability of the  $ET_a$  in the TP,  
139 and (3) uncover the main factors dominating the changes in  $ET_a$ , using the  
140 estimated product.

141

## 142 **2 Methodology and data**

### 143 **2.1 Model description**

144 The SEBS model ([Su, 2002](#)) was used to derive land surface energy flux  
145 components in the present study. The remote-sensed land surface energy  
146 balance equation is given by

147 
$$R_n = H + LE + G_0. \quad (1)$$

148  $R_n$  is net radiation flux ( $W m^{-2}$ ),  $H$  is sensible heat flux ( $W m^{-2}$ ),  $LE$  is latent  
 149 heat flux ( $W m^{-2}$ ), and  $G_0$  is ground heat flux ( $W m^{-2}$ ). Note that this equation  
 150 neglected energy stored in the canopy, energy consumption related to freeze-  
 151 thaw processes of permafrost and glacier, etc. Thus, this equation is  
 152 applicable without considering the phase change of water.

153

154 The land surface net radiation flux was computed as

155 
$$R_n = (1 - \alpha) \times SWD + LWD - \varepsilon \times \sigma \times T_s^4 \quad (2)$$

156 where  $\alpha$  is the land surface albedo derived from the Moderate Resolution  
 157 Imaging Spectroradiometer (MODIS) products. Downward shortwave ( $SWD$ )  
 158 and longwave ( $LWD$ ) radiation were obtained from the China Meteorological  
 159 Forcing Dataset (CMFD). Land surface temperature ( $T_s$ ) and emissivity ( $\varepsilon$ )  
 160 values were also obtained from MODIS products.

161

162 In vegetated areas the soil heat flux,  $G_0$ , was calculated from the net radiation  
 163 flux and vegetation cover

164 
$$G_0 = R_n \times (r_c \times f_c + r_s \times (1 - f_c)). \quad (3)$$

165  $r_s$  and  $r_c$  are ratios of ground heat flux and net radiation for surfaces with bare  
 166 soil and full vegetation, respectively. Fractional vegetation cover ( $f_c$ ) was  
 167 derived from the normalized difference vegetation index (NDVI). Over water  
 168 surfaces ( $NDVI < 0$  and  $\alpha < 0.47$ ),  $G_0 = 0.5R_n$  was used ([Gao et al., 2011](#);  
 169 [Chen et al., 2013a](#)). On glaciers,  $G_0$  is negligible ([Yang et al., 2011](#)) and  $G_0 =$   
 170  $0.05R_n$ .

171

172 In the atmospheric surface layer, sensible heat flux and friction velocity were  
 173 calculated based on the Monin-Obukhov similarity ([Stull, 1988](#)),

174 
$$U = \frac{u_*}{\kappa} \left[ \ln \left( \frac{z-d_0}{z_{0m}^{eff}} \right) - \psi_m \left( \frac{z-d_0}{L} \right) + \psi_m \left( \frac{z_{0m}^{eff}}{L} \right) \right] \quad (4)$$

175 
$$\theta_0 - \theta_a = \frac{H}{\kappa u_* \rho C_p} \left[ \ln \left( \frac{z-d_0}{z_{0h}^{eff}} \right) - \psi_h \left( \frac{z-d_0}{L} \right) + \psi_h \left( \frac{z_{0h}^{eff}}{L} \right) \right] \quad (5)$$

176 
$$L = \frac{\rho C_p u_*^3 \theta_v}{\kappa g H}. \quad (6)$$

177  $U$  is the horizontal wind velocity at a reference height  $z$  (m) above the ground  
 178 surface,  $\theta_0$  is the potential temperature at the land surface (K),  $\theta_a$  is the  
 179 potential temperature (K) at the reference height  $z$ ,  $d_0$  is the zero-plane  
 180 displacement height (m),  $\rho$  is the air density ( $\text{kg m}^{-3}$ ),  $C_p$  is the specific heat for  
 181 moist air ( $\text{J kg}^{-1} \text{ }^\circ\text{C}^{-1}$ ),  $\kappa = 0.4$  is the von Kármán's constant,  $u_*$  is the friction  
 182 velocity,  $L$  is the Monin-Obukhov length (m),  $\theta_v$  is the potential virtual  
 183 temperature (K) at the reference height  $z$ ,  $\psi_m$  and  $\psi_h$  are the stability  
 184 correction functions for momentum and sensible heat transfer respectively,  
 185 and  $g$  is the gravity acceleration ( $\text{m s}^{-2}$ ). To account for the form drag caused  
 186 by subgrid-scale topographical obstacles, effective roughness lengths for  
 187 momentum ( $z_{0m}^{eff}$ , m) and sensible heat ( $z_{0h}^{eff}$ , m) transfer were introduced into  
 188 the SEBS model by [Han et al. \(2017\)](#). These modifications are parameterized  
 189 as follows ([Grant and Mason, 1990](#); [Han et al., 2015](#)),

190 
$$\ln^2(h/2z_{0m}^{eff}) = \frac{\kappa^2}{0.5D\lambda + \kappa^2 / \ln^2(h/2z_{0m})} \quad (7)$$

191 
$$\ln(h/2z_{0h}^{eff} + 1) = \ln(h/2z_{0h} + 1) \frac{\ln(h/2z_{0m} + 1)}{\ln(h/z_{0m}^{eff} + 1)} \quad (8)$$

192 where  $h$  is the average height of the subgrid-scale roughness obstacles,  $\lambda$  is  
 193 the average density of the subgrid-scale roughness elements calculated from  
 194 digital elevation models,  $D$  is the form drag coefficient and  $D=0.4$  is used for  
 195 the mountainous areas of the TP as suggested by [Han et al. \(2015\)](#),  $z_{0m}$  and  
 196  $z_{0h}$  are the local-scale roughness lengths for momentum (m) and heat transfer  
 197 (m), respectively. Detailed calculations can be found in [Su \(2002\)](#). A revised  
 198 algorithm for  $z_{0h}$  developed by [Chen et al. \(2013b\)](#) was applied as this  
 199 algorithm outperforms the original scheme of the SEBS model on the TP.

200

201 To constraint the actual evapotranspiration, the evaporative fraction was



202 applied in the SEBS model, which is determined by taking energy balance  
203 considerations at dry and wet limiting cases. Under the dry-limit condition, the  
204 evaporation becomes zero due to the limited supply of available soil moisture,  
205 while water vapor evaporates at the potential rate under the wet-limit condition  
206 ([Su, 2002](#)). The evaporative fraction ( $\Lambda$ ) is defined as,

$$207 \quad \Lambda = \frac{LE}{R_n - G_0} \quad (9)$$

208 After calculating evaporative fraction based on the assumption of dry and wet  
209 limits, latent heat flux was calculated by inverting Equation (9). Finally, latent  
210 heat flux was converted to  $ET_a$ . Details are available in [Su \(2002\) and \(Chen](#)  
211 [et al., 2013a\)](#).

## 212 **2.2 Data**

213 In-situ observations, satellite-based products, and meteorological forcing data  
214 were used in this study to estimate monthly  $ET_a$  over the TP area. The CMFD,  
215 that was developed based on the released China Meteorological  
216 Administration (CMA) data ([He et al., 2020](#)), was used as model input. The  
217 CMFD covers the whole landmass of China at a spatial resolution of  $0.1^\circ$  and  
218 a temporal resolution of three hours. The CMFD dataset was established  
219 through the fusion of in-situ observations, remote sensing products, and  
220 reanalysis datasets. In particular, the dataset benefits from the merging of the  
221 observations at about 700 CMA's weather stations, and by using the Global  
222 Energy and Water Cycle Experiment – Surface Radiation Budget (GEWEX-  
223 SRB) shortwave radiation dataset ([Pinker and Laszlo, 1992](#)). The GEWEX-  
224 SRB data has not been used in any other reanalysis dataset. In addition,  
225 independent datasets observed in western China where weather stations are  
226 scarce were used to evaluate the CMFD. This includes data collected through  
227 the Heihe Watershed Allied Telemetry Experimental Research (HiWATER) ([Li](#)  
228 [et al., 2013](#)) and the Coordinated Enhanced Observing Period (CEOP) Asia-

229 Australia Monsoon Project (CAMP) ([Ma et al., 2003](#)). CMFD dataset has been  
230 validated against in situ meteorological observations and compared with other  
231 reanalysis datasets on the TP, demonstrating that it is one of the best  
232 meteorological forcing datasets over the TP area ([Zhou et al., 2016](#); [Xie et al.,  
233 2017](#); [Wang et al., 2020a](#)). Therefore, it is suitable for this study to drive the  
234 SEBS model. Detailed information for the CMFD dataset is listed in Table 1.

235

236 MODIS monthly land surface products, including land surface temperature  
237 and emissivity, land surface albedo, and vegetation index, provide land  
238 surface conditions for the SEBS model. Detailed information on MODIS land  
239 surface variables are listed in Table 1. The values of land surface variables in  
240 the MODIS monthly products are derived by compositing and averaging the  
241 values from the corresponding month of MODIS daily files. Validations of  
242 MODIS land surface temperature and albedo against in-situ observations on  
243 the TP suggesting a high quality of MODIS land surface products with low  
244 biases and small root-mean-square errors ([Wang et al., 2004](#); [Ma et al., 2011](#);  
245 [Chen et al., 2014](#)).

246

247 In-situ EC data observed at six flux stations on the TP were used to validate  
248 model results. Locations of the six observation sites are illustrated in Figure 1  
249 and detailed descriptions for these six sites are shown in Table 2. The  
250 instrumental setup at each site consists of: an EC system comprising a sonic  
251 anemometer (CSAT3, Campbell Scientific Inc) and an open-path gas analyzer  
252 (LI-7500, Li-COR); a four-component radiation flux system (CNR-1, Kipp &  
253 Zonen), installed at a height of 1.5 m; a soil heat flux plate (Hukseflux,  
254 HFP01), buried in the soil to a depth of 0.1 m; soil moisture and temperature  
255 probes, buried at a depth of 0.05, 0.10, and 0.15 m, respectively ([Han et al.,  
256 2017](#)). The EC data were processed with the EC software package TK3

257 ([Mauder and Foken, 2015](#)). The main post-processing procedures of the EC  
258 raw data were as follows: spike detection, coordinate rotation, spectral loss  
259 correction, frequency response corrections ([Moore, 1986](#)), and corrections for  
260 density fluctuations ([Webb et al., 1980](#)). The ground heat flux was obtained by  
261 summing the flux value observed by the heat flux plate and the energy  
262 storage in the layer above the heat flux plate ([Han et al., 2016](#)). A more  
263 comprehensive dataset including the EC data used in this work has been  
264 published and is freely available ([Ma et al., 2020](#)).

265

266 3-hourly CMFD data was averaged into daily and then into monthly data to be  
267 consistent with MODIS products in terms of temporal resolution. Daily land  
268 surface albedo has been averaged into monthly variable. MODIS land surface  
269 products and canopy height data were remapped onto CMFD's grid. Monthly  
270 EC data and in situ meteorological observations, which are used for model  
271 validation, were generated from half-hourly variables.

### 272 **2.3 Model evaluation metrics and data analysis methods**

273 The model performance was assessed using the Pearson correlation  
274 coefficient ( $R$ ), the root-mean-square error (RMSE), and the mean bias (MB)  
275 between the estimated and observed monthly  $ET_a$  at the six stations on the  
276 TP.

277

278 The least-square regression technique was used to detect the long-term linear  
279 annual trends in  $ET_a$  values. The linear model to simulate  $ET_a$  values ( $Y_t$ )  
280 against time ( $t$ ) is defined as below and the slope of the linear equation ( $b$ ) is  
281 taken as the changing trend,

$$282 \quad Y_t = Y_0 + bt + \varepsilon_t \quad (10)$$

283

284 The Student's *t*-test, having an  $n-2$  degree of freedom ( $n$  is the number of  
285 samples), was used to evaluate the statistical significance of the linear  
286 trends, and only tests with a  $p$ -value less than 0.05 were selected as having  
287 passed the significance test.

### 288 **3 Results and discussion**

#### 289 **3.1 Validation against flux tower observations**

290 The SEBS-estimated  $ET_a$  was validated against EC observations at six flux  
291 stations on the TP at a monthly scale (Figure 2). The SEBS model is capable  
292 of capturing both the magnitude and seasonal variation of the monthly  $ET_a$   
293 signal at all the six stations. The correlation coefficients are all larger than 0.9  
294 and have passed the significance test at the  $p = 0.01$  level. RMSE values  
295 range from 9.3 to 14.5 mm mo<sup>-1</sup> with the minimum at the BJ station and the  
296 maximum at the SETORS station. The MB values are all negative except at  
297 the NADORS station, which means the SEBS model slightly underestimated  
298  $ET_a$  values on the TP.

299

300 Specifically, the SEBS model performed particularly well at the short grass  
301 sites (BJ and NAMORS), with correlation coefficients as high as 0.98 and MB  
302 values below 5.0 mm mo<sup>-1</sup>. At the high grass site (SETORS) and the gravel  
303 site (QOMS), the SEBS model is capable of reproducing the EC-observed  
304 monthly  $ET_a$  with RMSE values of 14.5 and 13.2 mm mo<sup>-1</sup>, respectively. In  
305 addition, the underestimates of  $ET_a$  by SEBS are mostly in the dry season,  
306 when the canopy is withered. The validation at the site-scale indicates that the  
307 SEBS model used in this work can be applied to a wide range of ecosystems  
308 over the TP.

### 309 3.2 Spatial distribution

310 There was a clear spatial pattern to the multiyear average of annual  $ET_a$   
311 between 2001 and 2018 (Figure 3). In general, the SEBS-estimated  $ET_a$   
312 decreases from the southeast to the northwest of the TP, with the maximum  
313 value above 1200 mm in the southeastern Tibet and Hengduan Mountains  
314 and the minimum value less than 100 mm in the northwestern edge of the TP.  
315 In the central TP, where there are several lakes,  $ET_a$  was typically from 500 to  
316 1000 mm.  $ET_a$  was lower than 200 mm over the high, snow- and ice-bound,  
317 mountainous areas. For example, over the northern slopes of the Himalaya,  
318 Nyenchen Tanglha Mountains, and the eastern section of the Tanggula  
319 Mountains. The reason is that these snow- and ice-bound mountainous areas  
320 have a higher ability to reflect downward shortwave radiation and hence have  
321 less available energy to evaporate. On the whole, the domain averaged  
322 multiyear mean annual  $ET_a$  over the TP is  $496\pm 23$  mm. The total amount of  
323 water evapotranspired from the terrestrial surface of the TP are around  
324  $1238.3\pm 57.6$  km<sup>3</sup> yr<sup>-1</sup>, considering the area of the TP to be  $2.5\times 10^6$  km<sup>2</sup>.

325

326 Figure 4 shows the multi-year average spring (March, April, and May), summer  
327 (June, July, and August), autumn (September, October, and November), and  
328 winter (December, January, and February)  $ET_a$  on the TP. Generally, the  
329 distribution pattern of seasonal  $ET_a$  was comparable with that of the annual  
330  $ET_a$ . Both seasonal and annual  $ET_a$  show a decreasing trend from the  
331 southeastern TP to the northwestern TP. Note that the spatial contrast of  $ET_a$   
332 almost faded out in winter season owing to a minimum in available energy  
333 and precipitation (Figure 4d). The  $ET_a$  in spring is higher than that in autumn,  
334 except for some high mountainous areas (e.g.: mountain ranges of Himalaya  
335 and Hengduan mountains). The spring  $ET_a$  ranges from 50 mm to 450 mm,  
336 while autumn  $ET_a$  ranges from 50 mm to 250 mm. In summer, the  $ET_a$  is

337 larger than 250 mm in most of the TP, while the  $ET_a$  is still below 100 mm in  
338 large areas of the northwestern TP. The multiyear seasonal  $ET_a$  averaged  
339 over the whole TP is  $140\pm 10$  mm,  $256\pm 12$  mm,  $84\pm 5$  mm, and  $34\pm 4$  mm, for  
340 spring, summer, autumn, and winter, respectively.

### 341 **3.3 Trend analysis**

342 The trend of annual  $ET_a$  during 2001-2018 is shown in Figure 5. Overall, an  
343 increasing trend of SEBS-simulated  $ET_a$  is dominant in the eastern TP (lon >  
344  $90^\circ$  E) while a decreasing trend is dominant in the western TP (lon <  $90^\circ$  E).  
345 The trends pass the  $t$ -test ( $p < 0.05$ ) in most part of the areas. The decreasing  
346 trend in the western TP is pronounced and passes the  $t$ -test ( $p < 0.05$ ). This  
347 trend is larger than  $-7.5$  mm yr<sup>-1</sup> in most parts of the area and even larger than  
348  $-10$  mm yr<sup>-1</sup> in a few parts. In the eastern TP, the increasing trend is mostly  
349 between 5 and 10 mm yr<sup>-1</sup> and passes the  $t$ -test ( $p < 0.05$ ). The  $ET_a$  trend  
350 tends to be greater along the marginal region of the northern, eastern, and  
351 southeastern TP. Along the marginal region of the southwestern TP and in the  
352 western section of Himalaya Mountains this trend weakens.

353

354 The trends of seasonal  $ET_a$  between 2001 and 2018 are spatially  
355 heterogeneous over the TP (Figure 6). Decreasing trends in spring and  
356 summer are generally at a rate between  $-2.5$  and  $-7.5$  mm yr<sup>-1</sup>, and increasing  
357 trends are generally at a rate below 5.0 mm yr<sup>-1</sup> and 7.5 mm yr<sup>-1</sup> in spring and  
358 summer, respectively. Areas showing decreasing  $ET_a$  tend to become larger in  
359 autumn and winter seasons. Both the decreasing and increasing trends are  
360 subdued in autumn and winter compared with that in spring and summer  
361 seasons. Decreasing rates of  $ET_a$  in autumn and winter are generally below -  
362 2.5 mm yr<sup>-1</sup>, and only a few areas have a rate larger than  $-2.5$  mm yr<sup>-1</sup>.

363

364 Due to the contrast in the trends in the eastern and western halves of the TP,  
365 we divided the TP into two regions: the eastern TP (lon > 90° E) and the  
366 western TP (lon < 90° E). Trends of the  $ET_a$  anomaly averaged over the entire  
367 TP, the western TP, and the eastern TP are shown in Figure 7a. The domain  
368 means of  $ET_a$  on the TP as a whole, and in the western TP decreased at rates  
369 of  $-1.45 \text{ mm yr}^{-1}$  and  $-5.52 \text{ mm yr}^{-1}$ , respectively. However, the  $ET_a$  in the  
370 eastern TP increased at a rate of  $2.62 \text{ mm yr}^{-1}$ . The decreasing rate of  $ET_a$  in  
371 the entire TP is influenced mainly by the significant decrease of  $ET_a$  in the  
372 western TP. Seasonally, the rates of change of  $ET_a$  over the whole TP are -  
373  $0.82 \text{ mm yr}^{-1}$  ( $p < 0.05$ ) and  $-0.79 \text{ mm yr}^{-1}$  ( $p < 0.05$ ) in spring and summer,  
374 respectively (Figure 7b). However, in autumn and winter the  $ET_a$  changes at a  
375 rate of  $0.10 \text{ mm yr}^{-1}$  and  $0.06 \text{ mm yr}^{-1}$ , respectively, and do not pass the  $t$ -test  
376 ( $p < 0.05$ ).  $ET_a$  in spring and summer seasons account for 75.7% of the  
377 annual  $ET_a$ . The variation in amplitude and changing rates in these two  
378 seasons are much larger than in the other seasons. Moreover, spatial  
379 distributions of spring and summer  $ET_a$  trends are close to that of the annual  
380  $ET_a$  trend (Figure 6). Thus, changes of  $ET_a$  in the spring and summer  
381 dominate the variations of  $ET_a$  in the whole year.

382

383 The decrease of  $ET_a$  over the whole TP and in the western TP during 2001-  
384 2018 can be explained by the decrease of  $R_n$  in the same time period (Figure  
385 8a). From 2001 to 2012,  $ET_a$  averaged over the entire TP increased slightly  
386 and then decreased dramatically from 2012, reaching a minimum in 2014.  
387 The significant decrease in  $ET_a$  between 2012 and 2014 was due to the rapid  
388 decline of the  $R_n$  (Figure 8a). In the eastern TP,  $ET_a$  increased during 2001-  
389 2018, while  $R_n$  decreased in the same period. Thus,  $R_n$  was not the dominant  
390 factor controlling the annual variations of  $ET_a$ . However, the increasing trends  
391 of both precipitation and air temperature can explain the increase of  $ET_a$  in the

392 eastern TP during the period 2001-2018 (Figure 8b and Figure 8c). The  
393 increasing precipitation increased the water resource available for  $ET_a$ .  
394 Moreover, the increasing air temperature accelerated the melting of  
395 permafrost and glaciers on the TP. Hence, the melting water replenished the  
396 ecosystem and increased the  $ET_a$  of the eastern TP.

397

398 Although the domain-averaged trend in  $ET_a$  has been decreasing across the  
399 entire TP from 2001 to 2018,  $ET_a$  values in some areas have increased.  
400 Moreover, the changing rates also depend on the time series of  $ET_a$ . For  
401 example, the  $ET_a$  increased slightly from 2001 to 2012, while decreased from  
402 2001 to 2018. This demonstrates the necessity to evaluate the spatial  
403 distribution of changing trends in  $ET_a$  and utilize long time series to investigate  
404 the trends in  $ET_a$  over the TP.

#### 405 **4 Summary and conclusions**

406 The SEBS-estimated  $ET_a$  is at a resolution of around 10 km, while the  
407 footprint of EC observed  $ET_a$  values ranges from a few dozen meters to a few  
408 hundreds of meters. SEBS-estimated  $ET_a$  compares very well with  
409 observations at the six flux towers, showing low RMSE and MB values. These  
410 estimates were able to capture annual and seasonal variations in  $ET_a$ , despite  
411 these two datasets being mismatched in their spatial representation.

412

413 Heterogeneous land surface characteristics and nonlinear changes in  
414 atmospheric conditions resulted in heterogeneities in spatial distributions of  
415  $ET_a$  and changes in  $ET_a$ . The SEBS-estimated multiyear (2001-2018) mean  
416 annual  $ET_a$  on the TP was  $515 \pm 22$  mm, resulting in approximately  
417  $1287.5 \pm 55.0$  km<sup>3</sup> yr<sup>-1</sup> of total water evapotranspiration from the terrestrial  
418 surface. Annual  $ET_a$  generally decreased from the southeast to the northwest



419 of the TP. The maximum was over 1200 mm, in the southeastern Tibet and  
420 Hengduan Mountains, while the minimum was less than 100 mm in the  
421 northwest marginal area of the TP. Moreover,  $ET_a$  was typically lower than 200  
422 mm over snow- and ice-bound mountainous areas, as there was limited  
423 available energy to evaporate the water.

424

425 Averaged over the entire TP, annual  $ET_a$  increased slightly from 2001 to 2012,  
426 but decreased significantly after 2012 and reached a minimum in 2014.

427 Generally, there was a slight decreasing trend in the domain mean annual  $ET_a$   
428 on the TP at the rate of  $-1.45 \text{ mm yr}^{-1}$  ( $p < 0.05$ ) from 2001 to 2018. However,  
429 trends of annual  $ET_a$  were opposite in the western and eastern TP. The  
430 annual  $ET_a$  decreased significantly in the western TP at a rate of  $-5.52 \text{ mm yr}^{-1}$   
431 ( $p < 0.05$ ) from 2001 to 2018, while annual  $ET_a$  in the eastern TP increased  
432 at a rate of  $2.62 \text{ mm yr}^{-1}$  ( $p < 0.05$ ) in the same period.

433

434 The spatial distributions of seasonal  $ET_a$  trends were also noticeably  
435 heterogeneous during 2001-2018. The spatial patterns of  $ET_a$  trend in spring  
436 and summer were similar to the annual changes in  $ET_a$ .  $ET_a$  decreased as  
437 well in the spring and summer season but at slower rates compared with the  
438 annual  $ET_a$ , however, only very weak trends were found in the autumn and  
439 winter seasons.

440

## 441 **5 Data availability**

442 The dataset presented and analyzed in this article has been released and is  
443 available for free download from the Science Data Bank

444 (<http://www.dx.doi.org/10.11922/sciencedb.t00000.00010>, (Han et al., 2020))

445 and from the National Tibetan Plateau Data Center

446 (<https://data.tpdc.ac.cn/en/data/5a0d2e28-ebc6-4ea4-8ce4-a7f2897c8ee6/>).

447 The dataset is published under the Creative Commons Attribution 4.0

448 International (CC BY 4.0) license.

449

## 450 **Acknowledgments**

451 This study was funded by the Second Tibetan Plateau Scientific Expedition  
452 and Research (STEP) program (grant no. 2019QZKK0103), the Strategic  
453 Priority Research Program of Chinese Academy of Sciences (XDA20060101),  
454 the National Natural Science Foundation of China (91837208, 41705005, and  
455 41830650). The CMFD data were obtained from the National Tibetan Plateau  
456 Data Center ([https://data.tpdc.ac.cn/en/data/8028b944-daaa-4511-8769-  
457 965612652c49/](https://data.tpdc.ac.cn/en/data/8028b944-daaa-4511-8769-965612652c49/)). MODIS data were obtained from the NASA Land Processes  
458 Distributed Active Archive Center (<https://lpdaac.usgs.gov/>). Global 1 km  
459 forest canopy height data were obtained from the Oak Ridge National  
460 Laboratory Distributed Active Archive Center for Biogeochemical Dynamics  
461 ([https://daac.ornl.gov/cgi-bin/dsviewer.pl?ds\\_id=1271](https://daac.ornl.gov/cgi-bin/dsviewer.pl?ds_id=1271)). The authors would like  
462 to thank all colleagues working at the observational stations on the TP for their  
463 maintenance of the instruments.

464

465

- 467 Chen, X., Z. Su, Y. Ma, S. Liu, Q. Yu, Z. Xu. 2014. Development of a 10-year (2001-2010) 0.1° data set  
468 of land-surface energy balance for mainland China. *Atmospheric Chemistry and Physics* 14(23):  
469 13097-13117.
- 470 Chen, X., Z. Su, Y. Ma, E. M. Middleton. 2019. Optimization of a remote sensing energy balance method  
471 over different canopy applied at global scale. *Agricultural and Forest Meteorology* 279: 107633-  
472 107633.
- 473 Chen, X., Z. Su, Y. Ma, K. Yang, B. Wang. 2013a. Estimation of surface energy fluxes under complex  
474 terrain of Mt. Qomolangma over the Tibetan Plateau. *Hydrol. Earth Syst. Sci.* 17(4): 1607-1618.
- 475 Chen, X., Z. Su, Y. Ma, K. Yang, J. Wen, Y. Zhang. 2013b. An Improvement of Roughness Height  
476 Parameterization of the Surface Energy Balance System (SEBS) over the Tibetan Plateau. *Journal*  
477 *of Applied Meteorology and Climatology* 52(3): 607-622.
- 478 Fisher, J. B., F. Melton, E. Middleton, C. Hain, M. Anderson, R. Allen, M. F. McCabe, S. Hook, D.  
479 Baldocchi, P. A. Townsend, A. Kilic, K. Tu, D. D. Miralles, J. Perret, J.-P. Lagouarde, D. Waliser, A.  
480 J. Purdy, A. French, D. Schimel, J. S. Famiglietti, G. Stephens, E. F. Wood. 2017. The future of  
481 evapotranspiration: Global requirements for ecosystem functioning, carbon and climate feedbacks,  
482 agricultural management, and water resources. *Water Resources Research* 53(4): 2618-2626.
- 483 Gao, Z. Q., C. S. Liu, W. Gao, N. B. Chang. 2011. A coupled remote sensing and the Surface Energy  
484 Balance with Topography Algorithm (SEBTA) to estimate actual evapotranspiration over  
485 heterogeneous terrain. *Hydrol. Earth Syst. Sci.* 15(1): 119-139.
- 486 Grant, A. L. M., P. J. Mason. 1990. Observations of boundary-layer structure over complex terrain.  
487 *Quarterly Journal of the Royal Meteorological Society* 116(491): 159-186.
- 488 Han, C., Y. Ma, X. Chen, Z. Su. 2016. Estimates of land surface heat fluxes of the Mt. Everest region  
489 over the Tibetan Plateau utilizing ASTER data. *Atmospheric Research* 168: 180-190.
- 490 Han, C., Y. Ma, X. Chen, Z. Su. 2017. Trends of land surface heat fluxes on the Tibetan Plateau from  
491 2001 to 2012. *International Journal of Climatology* 37(14): 4757-4767.
- 492 Han, C., Y. Ma, Z. Su, X. Chen, L. Zhang, M. Li, F. Sun. 2015. Estimates of effective aerodynamic  
493 roughness length over mountainous areas of the Tibetan Plateau. *Quarterly Journal of the Royal*  
494 *Meteorological Society* 141(689): 1457-1465.
- 495 Han, C., Y. Ma, B. Wang, L. Zhong, W. Ma, X. Chen, Z. Su. 2020. The estimated actual  
496 evapotranspiration over the Tibetan Plateau from 2001 to 2018. *VI. Science Data Bank*.  
497 <http://www.dx.doi.org/10.11922/sciencedb.t00000.00010>.
- 498 He, J., K. Yang, W. Tang, H. Lu, J. Qin, Y. Chen, X. Li. 2020. The first high-resolution meteorological  
499 forcing dataset for land process studies over China. *Scientific Data* 7(1): 25-25.
- 500 Immerzeel, W. W., L. P. H. van Beek, M. F. P. Bierkens. 2010. Climate Change Will Affect the Asian  
501 Water Towers. *Science* 328(5984): 1382 LP-1385.
- 502 Li, X., G. Cheng, S. Liu, Q. Xiao, M. Ma, R. Jin, T. Che, Q. Liu, W. Wang, Y. Qi, J. Wen, H. Li, G. Zhu,  
503 J. Guo, Y. Ran, S. Wang, Z. Zhu, J. Zhou, X. Hu, Z. Xu. 2013. Heihe Watershed Allied Telemetry  
504 Experimental Research (HiWATER): Scientific Objectives and Experimental Design. *Bulletin of the*  
505 *American Meteorological Society* 94(8): 1145-1160.
- 506 Li, X., L. Wang, D. Chen, K. Yang, A. Wang. 2014. Seasonal evapotranspiration changes (1983–2006)

507 of four large basins on the Tibetan Plateau. *Journal of Geophysical Research: Atmospheres* 119(23):  
508 13,13-79,95.

509 Liu, X., H. Zheng, M. Zhang, C. Liu. 2011. Identification of dominant climate factor for pan evaporation  
510 trend in the Tibetan Plateau. *Journal of Geographical Sciences* 21(4): 594-608.

511 Ma, N., J. Szilagyi, Y. Zhang, W. Liu. 2019. Complementary-Relationship-Based Modeling of Terrestrial  
512 Evapotranspiration Across China During 1982–2012: Validations and Spatiotemporal Analyses.  
513 *Journal of Geophysical Research: Atmospheres* 124(8): 4326-4351.

514 Ma, W., Y. Ma, H. Ishikawa. 2014. Evaluation of the SEBS for upscaling the evapotranspiration based  
515 on in-situ observations over the Tibetan Plateau. *Atmospheric Research* 138: 91-97.

516 Ma, Y., Z. Hu, Z. Xie, W. Ma, B. Wang, X. Chen, M. Li, L. Zhong, F. Sun, L. Gu, C. Han, L. Zhang, X.  
517 Liu, Z. Ding, G. Sun, S. Wang, Y. Wang, Z. Wang. 2020. A long-term (2005–2016) dataset of hourly  
518 integrated land–atmosphere interaction observations on the Tibetan Plateau. *Earth Syst. Sci. Data*  
519 12(4): 2937-2957.

520 Ma, Y., Z. Su, T. Koike, T. Yao, H. Ishikawa, K. i. Ueno, M. Menenti. 2003. On measuring and remote  
521 sensing surface energy partitioning over the Tibetan Plateau—from GAME/Tibet to CAMP/Tibet.  
522 *Physics and Chemistry of the Earth, Parts A/B/C* 28(1): 63-74.

523 Ma, Y., L. Zhong, B. Wang, W. Ma, X. Chen, M. Li. 2011. Determination of land surface heat fluxes over  
524 heterogeneous landscape of the Tibetan Plateau by using the MODIS and in situ data. *Atmos. Chem.*  
525 *Phys.* 11(20): 10461-10469.

526 Mauder, M., T. Foken. 2015. Eddy-Covariance Software TK3.

527 Moore, C. J. 1986. Frequency response corrections for eddy correlation systems. *Boundary-Layer*  
528 *Meteorology* 37(1): 17-35.

529 Oki, T., S. Kanae. 2006. Global Hydrological Cycles and World Water Resources. *Science* 313(5790):  
530 1068 LP-1072.

531 Pinker, R. T., I. Laszlo. 1992. Modeling Surface Solar Irradiance for Satellite Applications on a Global  
532 Scale. *Journal of Applied Meteorology* 31(2): 194-211.

533 Shi, H., T. Li, G. Wang. 2017. Temporal and spatial variations of potential evaporation and the driving  
534 mechanism over Tibet during 1961–2001. *Hydrological Sciences Journal* 62(9): 1469-1482.

535 Stull, R. B. (1988). An introduction to boundary layer meteorology. Dordrecht, Kluwer Academic  
536 Publishers.

537 Su, Z. 2002. The Surface Energy Balance System (SEBS) for estimation of turbulent heat fluxes. *Hydrol.*  
538 *Earth Syst. Sci.* 6(1): 85-100.

539 Szilagyi, J., R. Crago, R. Qualls. 2017. A calibration-free formulation of the complementary relationship  
540 of evaporation for continental-scale hydrology. *Journal of Geophysical Research: Atmospheres*  
541 122(1): 264-278.

542 Wang, B., Y. Ma, Z. Su, Y. Wang, W. Ma. 2020a. Quantifying the evaporation amounts of 75 high-  
543 elevation large dimictic lakes on the Tibetan Plateau. *Science Advances* 6(26): eaay8558.

544 Wang, G., S. Lin, Z. Hu, Y. Lu, X. Sun, K. Huang. 2020b. Improving Actual Evapotranspiration  
545 Estimation Integrating Energy Consumption for Ice Phase Change Across the Tibetan Plateau.  
546 *Journal of Geophysical Research: Atmospheres* 125(3): e2019JD031799-e032019JD031799.

547 Wang, K., J. Liu, X. Zhou, M. Sparrow, M. Ma, Z. Sun, W. Jiang. 2004. Validation of the MODIS global  
548 land surface albedo product using ground measurements in a semidesert region on the Tibetan

549 Plateau. *Journal of Geophysical Research: Atmospheres* 109(D5).

550 Webb, E. K., G. I. Pearman, R. Leuning. 1980. Correction of flux measurements for density effects due  
551 to heat and water vapour transfer. *Quarterly Journal of the Royal Meteorological Society* 106(447):  
552 85-100.

553 Xie, Z., Z. Hu, L. Gu, G. Sun, Y. Du, X. Yan. 2017. Meteorological Forcing Datasets for Blowing Snow  
554 Modeling on the Tibetan Plateau: Evaluation and Intercomparison. *Journal of Hydrometeorology*  
555 18(10): 2761-2780.

556 Xu, C. Y., V. P. Singh. 2005. Evaluation of three complementary relationship evapotranspiration models  
557 by water balance approach to estimate actual regional evapotranspiration in different climatic  
558 regions. *Journal of Hydrology* 308(1): 105-121.

559 Yang, K., H. Wu, J. Qin, C. Lin, W. Tang, Y. Chen. 2014. Recent climate changes over the Tibetan Plateau  
560 and their impacts on energy and water cycle: A review. *Global and Planetary Change* 112: 79-91.

561 Yang, W., X. Guo, T. Yao, K. Yang, L. Zhao, S. Li, M. Zhu. 2011. Summertime surface energy budget  
562 and ablation modeling in the ablation zone of a maritime Tibetan glacier. *Journal of Geophysical*  
563 *Research: Atmospheres* 116(D14).

564 Yao, T., H. Lu, W. Feng, Q. Yu. 2019. Evaporation abrupt changes in the Qinghai-Tibet Plateau during  
565 the last half-century. *Scientific Reports* 9(1): 20181-20181.

566 Yao, T., L. Thompson, W. Yang, W. Yu, Y. Gao, X. Guo, X. Yang, K. Duan, H. Zhao, B. Xu, J. Pu, A. Lu,  
567 Y. Xiang, D. B. Kattel, D. Joswiak. 2012. Different glacier status with atmospheric circulations in  
568 Tibetan Plateau and surroundings. *Nature Climate Change* 2(9): 663-667.

569 Zhang, C., F. Liu, Y. Shen. 2018a. Attribution analysis of changing pan evaporation in the Qinghai-  
570 Tibetan Plateau, China. *International Journal of Climatology* 38(S1): e1032-e1043.

571 Zhang, K., J. S. Kimball, R. R. Nemani, S. W. Running. 2010. A continuous satellite-derived global  
572 record of land surface evapotranspiration from 1983 to 2006. *Water Resources Research* 46(9).

573 Zhang, T., M. Gebremichael, X. Meng, J. Wen, M. Iqbal, D. Jia, Y. Yu, Z. Li. 2018b. Climate-related  
574 trends of actual evapotranspiration over the Tibetan Plateau (1961–2010). *International Journal of*  
575 *Climatology* 38(S1): e48-e56.

576 Zhang, Y., C. Liu, Y. Tang, Y. Yang. 2007. Trends in pan evaporation and reference and actual  
577 evapotranspiration across the Tibetan Plateau. *Journal of Geophysical Research: Atmospheres*  
578 112(D12).

579 Zhong, L., Y. Ma, Z. Hu, Y. Fu, Y. Hu, X. Wang, M. Cheng, N. Ge. 2019. Estimation of hourly land  
580 surface heat fluxes over the Tibetan Plateau by the combined use of geostationary and polar-orbiting  
581 satellites. *Atmos. Chem. Phys.* 19(8): 5529-5541.

582 Zhou, J., L. Wang, Y. Zhang, Y. Guo, D. He. 2016. Spatiotemporal variations of actual evapotranspiration  
583 over the Lake Selin Co and surrounding small lakes (Tibetan Plateau) during 2003–2012. *Science*  
584 *China Earth Sciences* 59(12): 2441-2453.

585 Zou, M., L. Zhong, Y. Ma, Y. Hu, Z. Huang, K. Xu, L. Feng. 2018. Comparison of Two Satellite-Based  
586 Evapotranspiration Models of the Nagqu River Basin of the Tibetan Plateau. *Journal of Geophysical*  
587 *Research: Atmospheres* 123(8): 3961-3975.

588

589

590 **List of tables**

591 Table 1: Input datasets used in this study. .... 23

592 Table 2: Station information. .... 24

593

594

595

596 Table 1: Input datasets used in this study.

<b>Variables</b>	<b>Data source</b>	<b>Availability</b>	<b>Temporal resolution</b>	<b>Spatial resolution</b>
Downward Shortwave	CMFD	1979 – 2018	3 hours	0.1°
Downward longwave	CMFD	1979 – 2018	3 hours	0.1°
Air temperature	CMFD	1979 – 2018	3 hours	0.1°
Specific humidity	CMFD	1979 – 2018	3 hours	0.1°
Wind velocity	CMFD	1979 – 2018	3 hours	0.1°
Land surface temperature	MOD11C3	2001 – now	Monthly	0.05°
Land surface emissivity	MOD11C3	2001 – now	Monthly	0.05°
Height of canopy	GLAS & SPOT	2000 - now	Monthly	0.01°
Albedo	MOD09CMG	2001 - now	Daily	0.05°
<i>NDVI</i>	MOD13C2	2001 - now	Monthly	0.05°
DEM	ASTER GDEM	-	-	30 m

597

598

599

600 Table 2: Station information.

<b>Station</b>	<b>Location</b>	<b>Elevation (m)</b>	<b>Land cover</b>
QOMS	28.21°N, 86.56°E	4276	Gravel
NAMORS	30.46°N, 90.59°E	4730	Grassy marshland
SETORS	29.77°N, 94.73°E	3326	Grass land
NADORS	33.39°N, 79.70°E	4264	Sparse grass-Gobi
MAWORS	38.41°N, 75.05°E	3668	Sparse grass-Gobi
BJ	31.37°N, 91.90°E	4509	Sparseness meadow

601

602

603

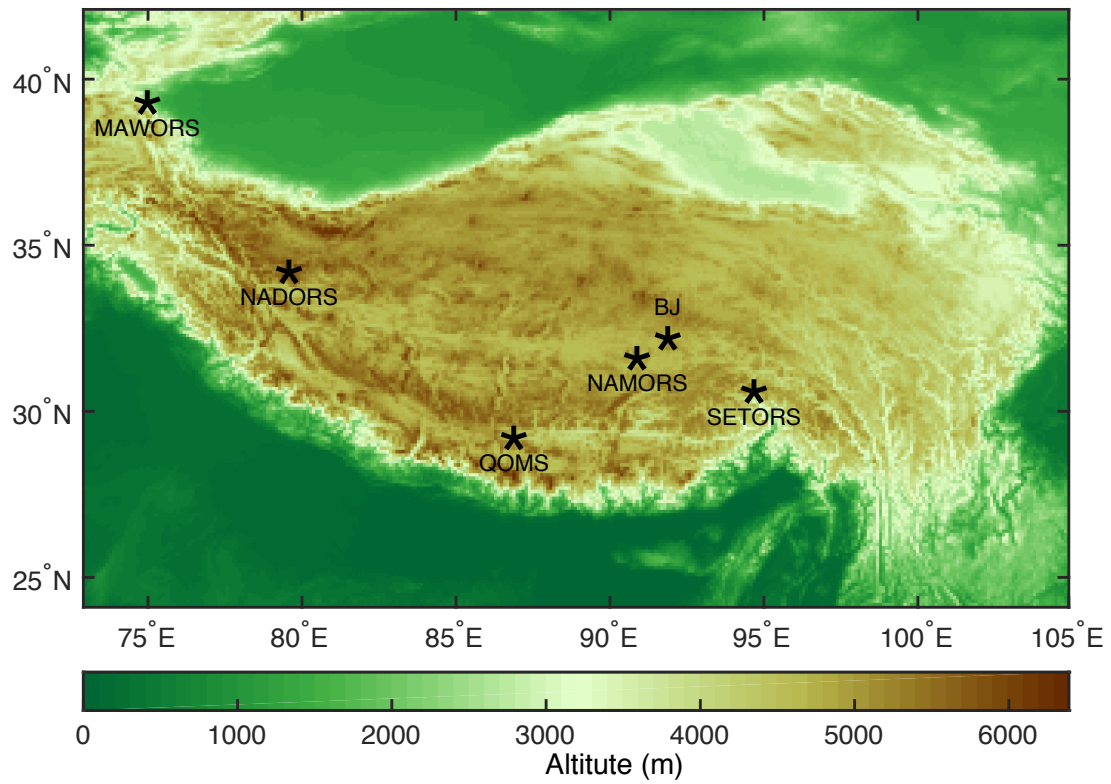


604

## List of figures

605	Figure 1: Locations of the six flux tower sites (marked by pentagrams) on the	
606	TP. The legend of the color map is elevation above mean sea level in meters.	
607	.....	26
608	Figure 2: SEBS-estimated and EC-observed monthly $ET_a$ at the six stations (a-	
609	f) on the TP in years when the latter observations were available. RMSE is the	
610	root-mean-square error, MB is the mean bias, and R is the correlation	
611	coefficient. ....	27
612	Figure 3: Spatial distribution of the SEBS-estimated multiyear (2001-2018)	
613	average annual $ET_a$ . ....	28
614	Figure 4: Spatial distributions of the SEBS-estimated multiyear (2001-2018)	
615	average seasonal $ET_a$ (mm/season) values over the TP. (a) spring, (b) summer,	
616	(c) autumn, (d) winter. ....	29
617	Figure 5: Spatial distribution of annual $ET_a$ linear trend on the TP from 2001 to	
618	2018. The stippling indicates the trends that pass the t-test ( $p < 0.05$ ). ....	30
619	Figure 6: Spatial distributions of seasonal $ET_a$ linear trends on the TP from 2001	
620	to 2018: (a) annual, (b) spring, (c) summer, (d) autumn, (e) winter. The stippling	
621	indicates the trends that pass the t-test ( $p < 0.05$ ). ....	31
622	Figure 7: Anomalies of the domain-averaged annual $ET_a$ of the entire TP, the	
623	western TP ( $\text{lon} < 90^\circ \text{ E}$ ), and the eastern TP ( $\text{lon} > 90^\circ \text{ E}$ ), respectively (a).	
624	Domain-averaged seasonal $ET_a$ anomalies over the entire TP (b). The dashed	
625	straight lines indicate linear trends during 2001-2018, and $k$ is the slope of the	
626	straight line. ....	32
627	Figure 8: Domain-averaged anomalies of annual $R_n$ (a), precipitation (b), and	
628	temperature (c) over the entire TP, the western TP ( $\text{lon} < 90^\circ \text{ E}$ ), and the eastern	
629	TP ( $\text{lon} > 90^\circ \text{ E}$ ), respectively. The dashed straight lines indicate linear trends	
630	during 2001-2018, and $k$ is the slope of the straight line. ....	33
631		

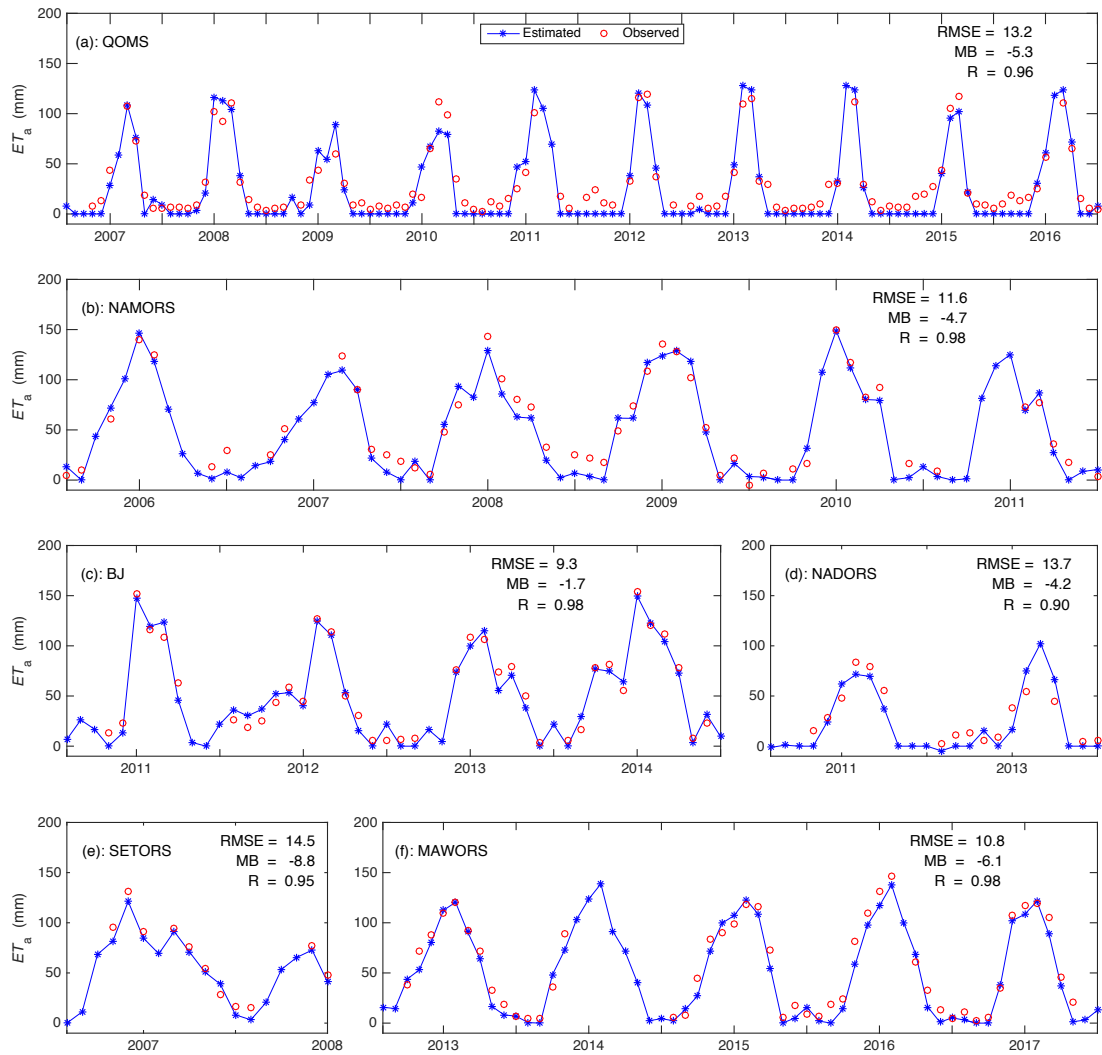
632



633

634 Figure 1: Locations of the six flux tower sites (marked by pentagrams) on the  
635 TP. The legend of the color map is elevation above mean sea level in meters.

636

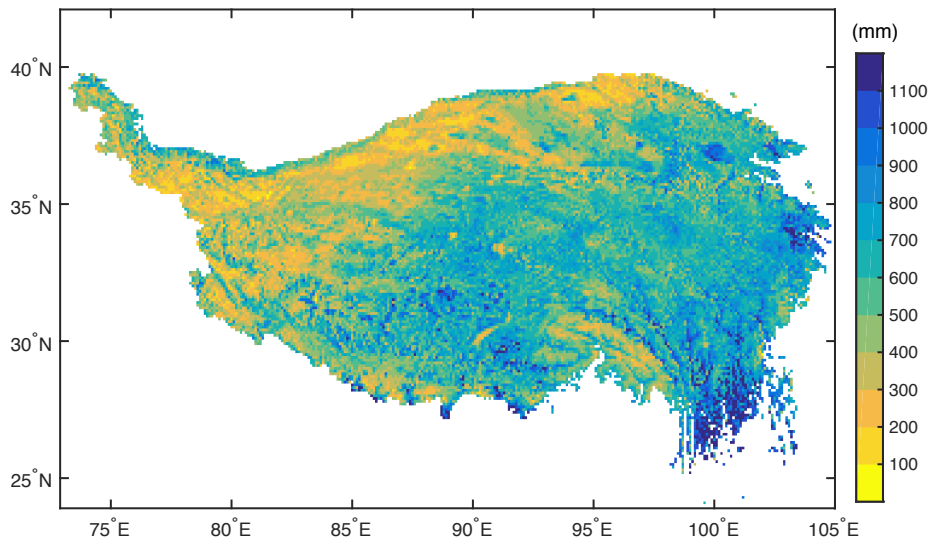


638

639 Figure 2: SEBS-estimated and EC-observed monthly  $ET_a$  at the six stations  
 640 (a-f) on the TP in years when the latter observations were available. RMSE is  
 641 the root-mean-square error, MB is the mean bias, and R is the correlation  
 642 coefficient.

643

644

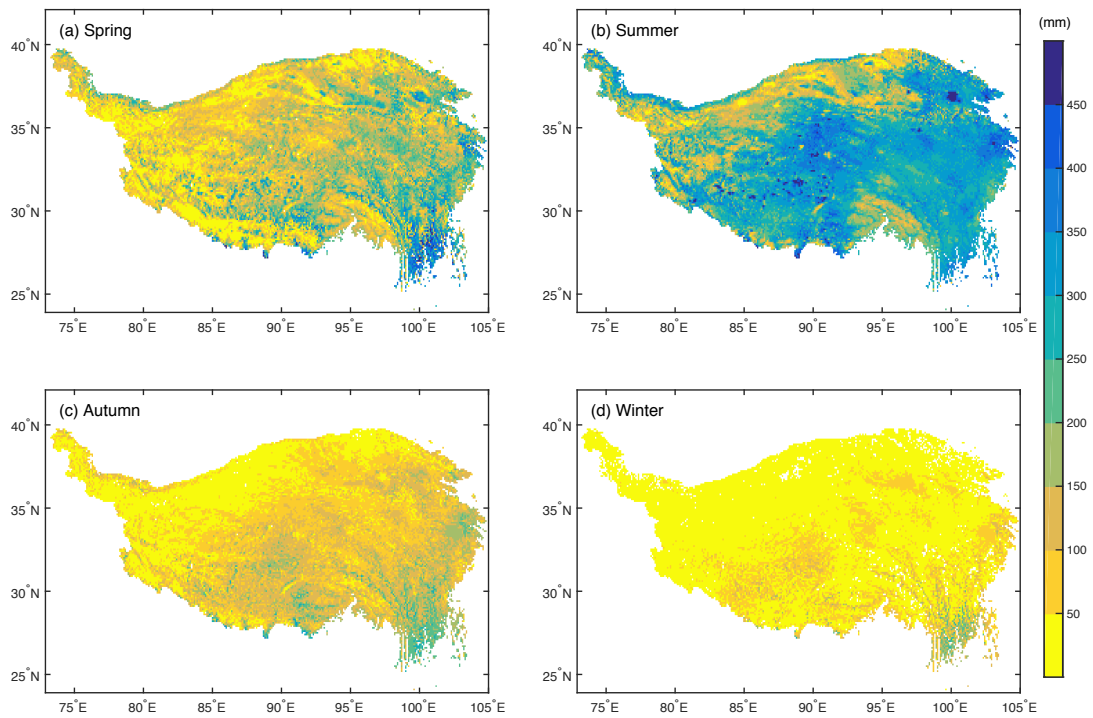


645

646 Figure 3: Spatial distribution of the SEBS-estimated multiyear (2001-2018)

647 average annual  $ET_a$ .

648



650

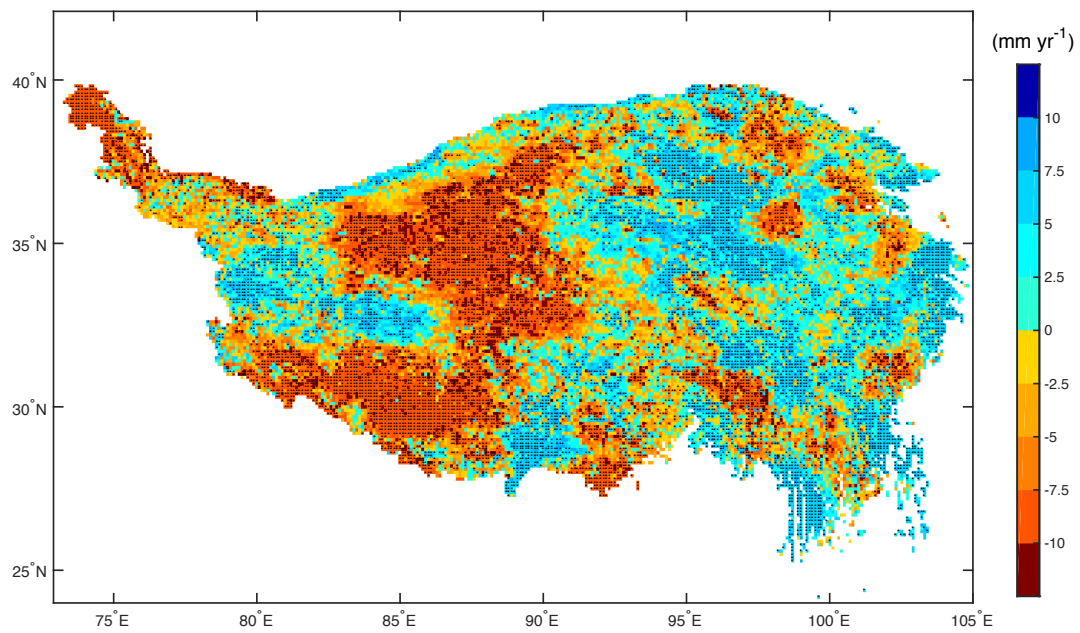
651 Figure 4: Spatial distributions of the SEBS-estimated multiyear (2001-2018)

652 average seasonal  $ET_a$  (mm/season) values over the TP. (a) spring, (b)

653 summer, (c) autumn, (d) winter.

654

655

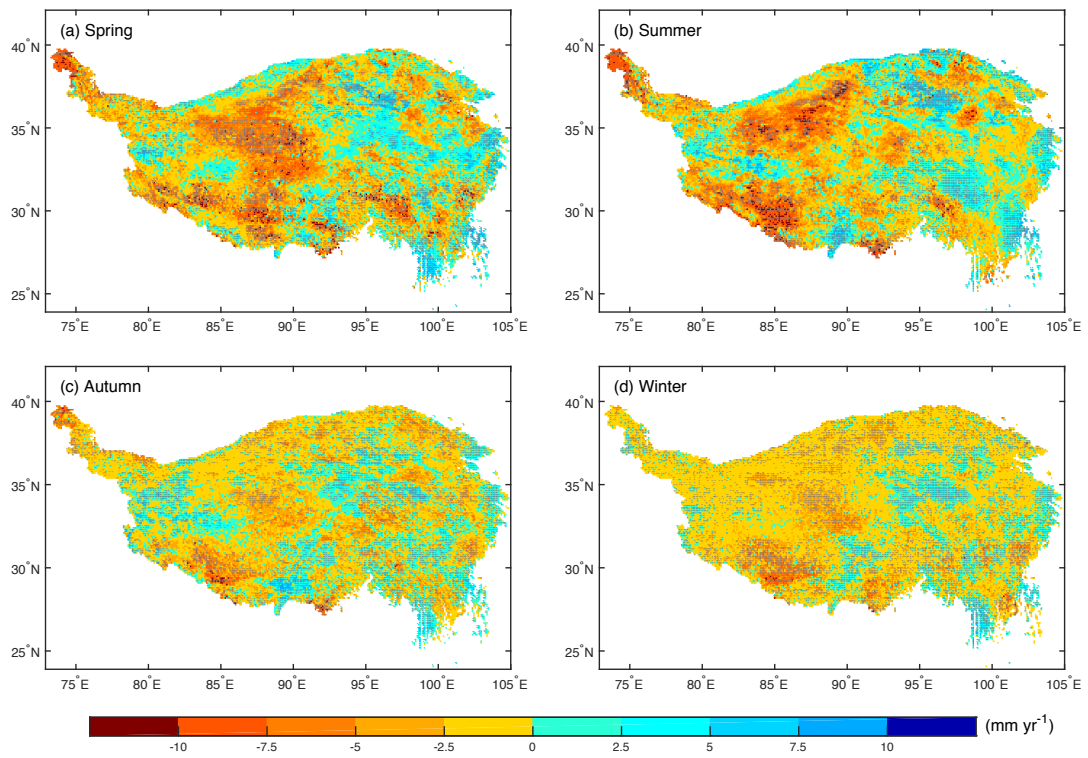


656

657 Figure 5: Spatial distribution of annual  $ET_a$  linear trend on the TP from 2001 to

658 2018. The stippling indicates the trends that pass the t-test ( $p < 0.05$ ).

659

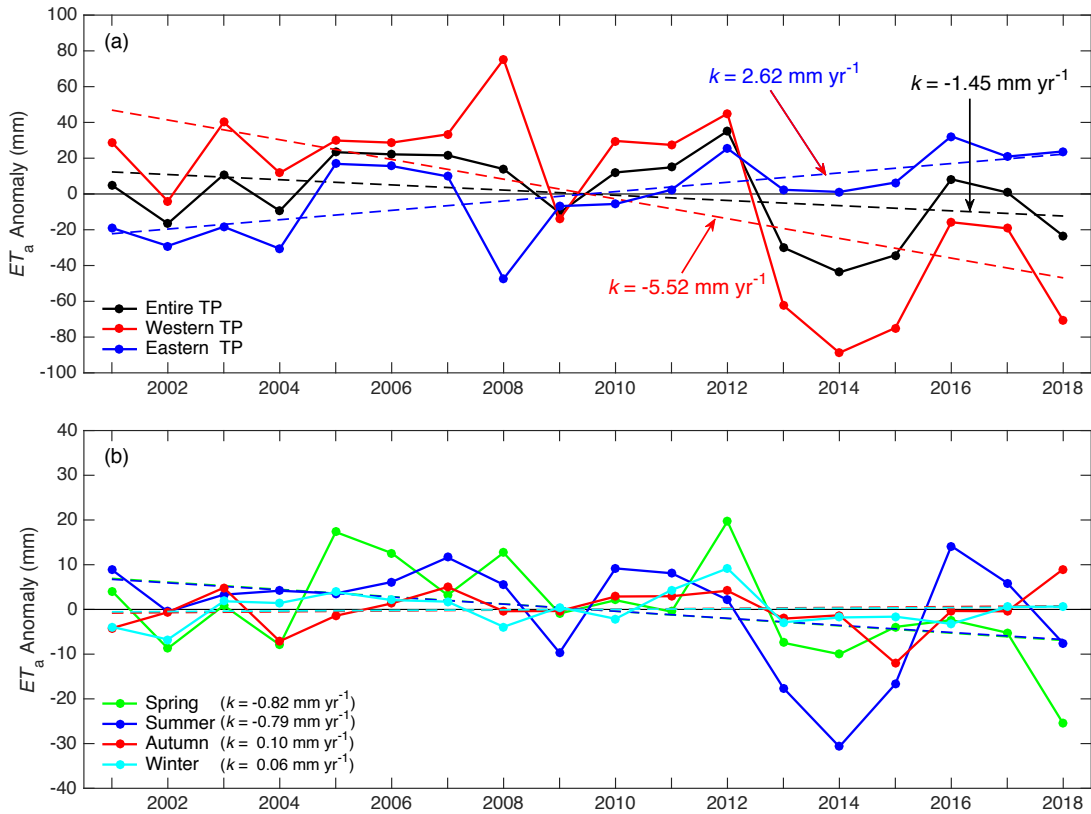


661

662 Figure 6: Spatial distributions of seasonal  $ET_a$  linear trends on the TP from  
 663 2001 to 2018: (a) annual, (b) spring, (c) summer, (d) autumn, (e) winter. The  
 664 stippling indicates the trends that pass the  $t$ -test ( $p < 0.05$ ).

665

666



667

668 Figure 7: Anomalies of the domain-averaged annual  $ET_a$  of the entire TP, the  
669 western TP (lon < 90° E), and the eastern TP (lon > 90° E), respectively (a).

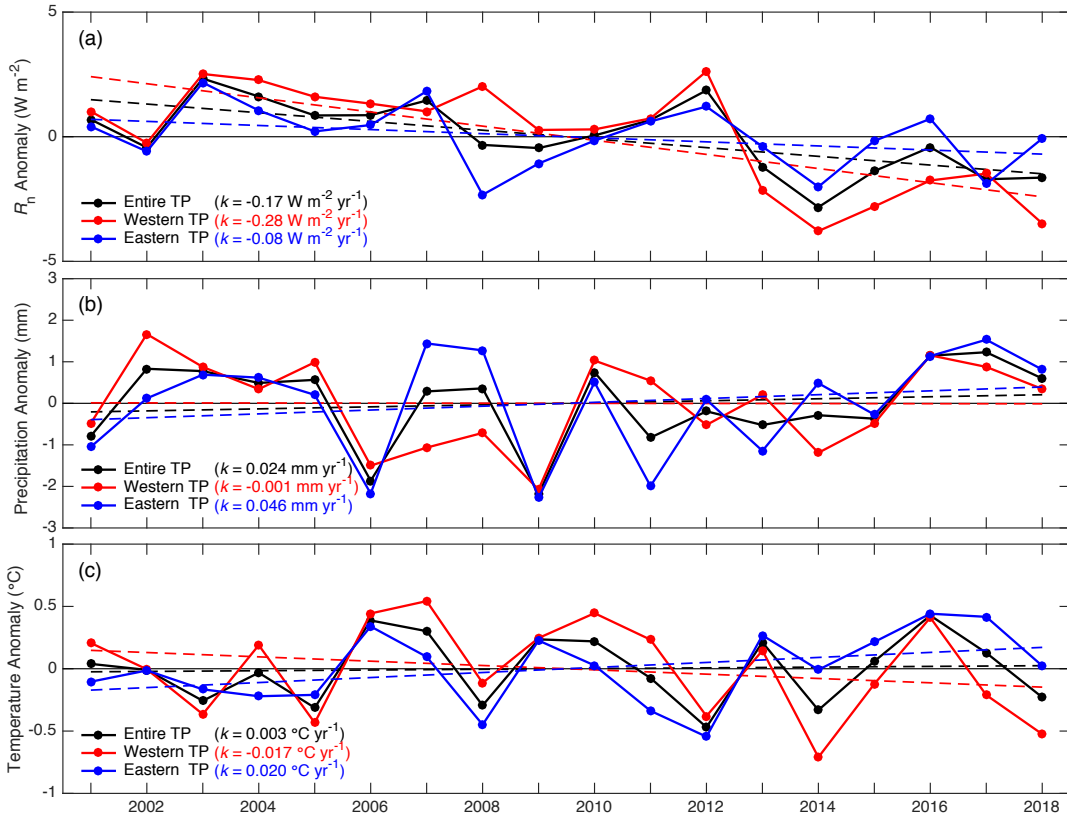
670 Domain-averaged seasonal  $ET_a$  anomalies over the entire TP (b). The dashed  
671 straight lines indicate linear trends during 2001-2018, and  $k$  is the slope of the  
672 straight line.

673

674



675



676

677 Figure 8: Domain-averaged anomalies of annual  $R_n$  (a), precipitation (b), and  
678 temperature (c) over the entire TP, the western TP ( $lon < 90^{\circ} E$ ), and the  
679 eastern TP ( $lon > 90^{\circ} E$ ), respectively. The dashed straight lines indicate  
680 linear trends during 2001-2018, and  $k$  is the slope of the straight line.

681